

Article

The Effect of Different g-C₃N₄ Precursor Nature on Its Structural Control and Photocatalytic Degradation Activity

Xiuhang Liu ^{1,†}, Xiaoye Xu ^{1,†}, Huihui Gan ^{1,2,*}, Mengfei Yu ¹ and Ying Huang ^{1,*}¹ School of Civil and Environmental Engineering, Ningbo University, Ningbo 315211, China² Institute of Ocean Engineering, Ningbo University, Ningbo 315211, China

* Correspondence: ganhuihui@nbu.edu.cn (H.G.); huangying1@nbu.edu.cn (Y.H.)

† These authors have contributed equally to this work and share first authorship.

Abstract: Due to its good visible-light photocatalytic activity and environmental friendliness, g-C₃N₄ has attracted much attention. The relationship between precursor type and the properties of obtained catalysts is interesting to investigate. In this work, target catalysts were prepared via the thermal polymerization of different precursors, melamine, a mixture of urea and melamine, and a mixture of melamine and cyanuric acid. The prepared g-C₃N₄ were characterized by X-ray diffraction (XRD), Fourier transform infrared spectrometry (FT-IR), UV-vis diffuse reflectance spectroscopy (UV-vis DRS), and scanning electron microscopy (SEM). Through the characterization and analysis, the adjusting of precursors could result in the change of the microstructure. The maximum BET surface area was 98.04 cm³g⁻¹ through precursor controlling, more than eight times that of MCN (11.15 cm³g⁻¹) using melamine as precursor. The thermal decomposition process was also analyzed to discuss the interaction and polymerization with precursor controlling. The introduction of melamine and cyanuric acid with melamine as precursors led to the formation of a special nanotube structure and additional function groups on the surface of g-C₃N₄ to increase the photocatalytic activity.

Keywords: g-C₃N₄; photocatalytic activity; precursors; microstructure; antibiotics



Citation: Liu, X.; Xu, X.; Gan, H.; Yu, M.; Huang, Y. The Effect of Different g-C₃N₄ Precursor Nature on Its Structural Control and Photocatalytic Degradation Activity. *Catalysts* **2023**, *13*, 848. <https://doi.org/10.3390/catal13050848>

Academic Editors: Sheng Guo, Yazi Liu and Jun Li

Received: 27 March 2023

Revised: 27 April 2023

Accepted: 4 May 2023

Published: 7 May 2023



Copyright: © 2023 by the authors. Licensee MDPI, Basel, Switzerland. This article is an open access article distributed under the terms and conditions of the Creative Commons Attribution (CC BY) license (<https://creativecommons.org/licenses/by/4.0/>).

1. Introduction

Antibiotics, as an antimicrobial drug and growth promoter, are widely used in human clinical and veterinary drugs. Since the outbreak of COVID-19, human dependence on antibiotics has expanded, and the abuse of antibiotics has become more and more serious [1]. Various antibiotics have been frequently detected in natural bodies of water [2,3], which is a serious problem for the ecological environment and human health.

In recent years, the advanced oxidation process (AOPs) has attracted significant attention because of its fast reaction rate, efficient high-concentration wastewater treatment, and high degree of mineralization. AOPs was proposed to produce highly oxidized hydroxyl radicals to mineralize pollutants. This technology has also developed a variety of processes, which can be distinguished according to different oxidants, such as ozone oxidation with ozone (O₃) [4], Fenton oxidation with hydrogen peroxide (H₂O₂) [5], and persulfate with persulfate [6]. Photocatalytic oxidation technology can directly use light energy to produce oxidation-free radicals. Compared with other methods, it possesses the advantages of being more green, efficient, and low cost, showing a good application prospect in antibiotic wastewater treatment. Preparing high efficiency photocatalysts or improving photocatalysts through specific technology is essential for photocatalytic technology, which is also the focus of current research.

Carbon nitride (C₃N₄) as a metal-free polymeric material has attracted much attention and has been considered a promising photocatalyst because of its unique electronic properties [7–10]. There are several allotropes for C₃N₄, in which the graphitic carbon nitride (g-C₃N₄) is regarded as the most stable form and most intensively studied [11].

In recent years, g-C₃N₄ has increasingly developed in many fields, such as water splitting [12], heavy metal adsorption [13], pollutant degradation [14], and bacteria disinfection [15]. Since g-C₃N₄ was widely concerned, researchers at home and abroad began to invest a lot of energy and try various means to synthesize this new material.

Up to now, the commonly used preparation methods include thermal polymerization, supramolecular self-assembly, solvent thermal synthesis, high temperature and high-pressure synthesis, electrochemical deposition, and physical/chemical vapor deposition. Wang et al. [16] synthesized a O-doped g-C₃N₄ catalyst by the solvothermal method at a relatively low temperature. By this template-free way, they obtained hollow microspheres of O-doped g-C₃N₄, which showed good photocatalytic activity for the pollutant degradation and water hydrogen decomposition. Chebanenko et al. [17] deposited g-C₃N₄-based composites by oxide process vapor deposition (OPVD), which can be used as a multi-junction carbon photocatalyst owing to a wider working spectrum. Wang et al. [18], using melamine as a precursor and three-dimensional cubic mesoporous silica KIT-6 as a template, prepared ordered cubic mesoporous g-C₃N₄ by simple chemical vapor deposition. The obtained ordered mesoporous g-C₃N₄ showed higher photocatalytic activity than sheet g-C₃N₄ in the reduction of CO₂ and H₂O. Liu et al. [19] prepared C-doped hollow spherical g-C₃N₄ derived from supramolecular self-assembly of melamine, glucose, and cyanuric acid, which exhibited enhanced photoredox water-splitting with a hydrogen yield of 305 mmol h⁻¹, 28.5 times than that of bulk g-C₃N₄.

Among various synthesis methods of g-C₃N₄, thermal polymerization is a facile method with no additive except the precursor itself. The N-rich molecular precursors such as melamine, urea, and thiourea have been widely used for photocatalysis. However, the g-C₃N₄ obtained from polycondensation reactions of melamine has many limits, such as the low specific surface area and a high charge carrier recombination rate under solar-light excitation, resulting in low photocatalytic activity.

Recently, there are many attempts at improving the photocatalytic performance of g-C₃N₄, such as doping metal elements, coupling with other semiconductors, and nanostructure engineering. Element doping can adjust the valence band and conduction band potential of materials, thus improving the photocatalytic performance. P/Cl co-doped carbon nitride nanosheets with nitrogen defects were prepared by one-step heat treatment [20]. P and Cl atoms successfully entered the structural units of g-C₃N₄, creating more defects simultaneously. These newly generated defects can significantly improve the photocatalytic performance of g-C₃N₄. The prepared materials show more efficient and stable photocatalytic activity for the photocatalytic decomposition of RhB and NOR under visible light irradiation. Chang et al. [21] prepared Pd-doped mesoporous g-C₃N₄ and used it to degrade bisphenol A in water. The surface doping with Pd can improve the optical absorption of mesoporous g-C₃N₄ in the UV-vis range. When it comes to material coupling, it is regarded as a practical approach to promote charge separation of photoexcited electron-hole pairs. Coupling with other semiconductors is a good approach to forming a highly efficient transport path for the photogenerated electron-hole pairs. Cao et al. [22] reported that the g-C₃N₄/WO₃ nanoplate composite, showed as a direct solid-state Z-scheme heterojunction, drastically improved the photocatalytic efficiency for NO removal, which was approximately 2.1 times higher than that of pure g-C₃N₄. Tang et al. [23] successfully synthesized TiO₂/g-C₃N₄ composite nanofiber materials by electrospinning with titanium n-butyl ether and urea. Under visible-light irradiation, the degradation rate of rhodamine B by the composite was 6.4 times higher than that of pure g-C₃N₄.

Besides the mentioned modifying strategies, the microstructure fabrication of g-C₃N₄ has been an effective method to boost its photocatalytic performance. The porous structure in morphology regulation has a higher surface area, porosity, and carrier separation and mobility than the block g-C₃N₄, thus improving its photocatalytic activity. Liang et al. [24] obtained ultra-thin g-C₃N₄ nanosheets with large carbon vacancies and higher specific surface area by heat-treating bulk g-C₃N₄ under NH₃, and the transfer and diffusion rate of photoelectron-hole pairs were significantly improved. Self-templating of melamine with

urea, cyanuric acid, and cyanuric chloride, is a simple, safe, and cheap method to tune porous and hollow microstructures, such as nanorods [25], nanosheets [26], nanoflower [27], and nanotubes [28] of $g\text{-C}_3\text{N}_4$. In addition, the aggregates can be generated from melamine and other N-rich molecular precursors through noncovalent interactions, such as hydrogen bonding, to form well-organized $g\text{-C}_3\text{N}_4$ precursors. Therefore, it is significant to explore the influence of different precursors on the microstructure and photocatalytic activity of $g\text{-C}_3\text{N}_4$ to understand further the microstructure of carbon nitride and its influence on photocatalytic efficiency.

The photocatalytic activity of the prepared catalyst was evaluated by the decomposition of norfloxacin (NOR) antibiotics in solution. NOR, as a quinolone antibiotic, is widely used in medical and animal husbandry fields. However, NOR usually has an incomplete metabolism in organisms; 60–90% in the form of original agents or metabolites are excreted into the environment, and with the natural water circulation migration to surface water, groundwater, and even drinking water, causing serious harm to the aquatic ecosystem and human health [29–31]. Nowadays, reducing the release of antibiotics into aquatic environments is an urgent concern. In addition, antibiotics were proven to be particularly resistant to wastewater treatment.

In this work, $g\text{-C}_3\text{N}_4$ was synthesized by the thermal decomposition of melamine, a mixture of urea and melamine, and a mixture of melamine and cyanuric acid as precursors, respectively. As a method to study the thermodynamic behavior of materials, thermal decomposition kinetics is expected to solve the relationship between precursor structure and target catalyst structure. The thermal decomposition kinetics were studied using thermogravimetry (TG) to further analyze the differences in thermal polymerization by using melamine as a single precursor and combined precursors for the preparation of $g\text{-C}_3\text{N}_4$. The changing micro-morphology by controlling precursors was also discussed. This paper aims to reveal the effect of adjusting precursors on the microstructure of target products and visible-light photocatalytic activity for the degradation of NOR in solution.

2. Results and Discussion

2.1. Structure and Morphology of $g\text{-C}_3\text{N}_4$ Prepared by Different Precursors

The crystal structure of the prepared $g\text{-C}_3\text{N}_4$ samples including MCN, UMCN, and CMCN was studied by XRD. The thermal decomposition of melamine synthesized the catalyst samples, denoted as MCN. The obtained samples using a mixture of urea and melamine or a combination of melamine and cyanuric acid as precursors were denoted as UMCN and CMCN, respectively. As shown in Figure 1, the characteristic peaks of all $g\text{-C}_3\text{N}_4$ samples were similar. The sharp and strong peak at about 27.6° assigned to the (002) facet of $g\text{-C}_3\text{N}_4$ was associated with the stacking of the conjugated aromatic sheets. Another characteristic peak at 13.1° assigned to the (100) facet was ascribed to in-plane nitrogen linkages of tri-s-triazine motifs. In addition, the peak intensity of UMCN was dramatically lower than that of MCN and CMCN, implying the decrease of crystal growth and a looser structure through the involvement of urea. As previously reported [32], during the decomposition processes of the urea, a large amount of NH_3 formed. This small and polar molecule could intercalate into the interplanar space and break the weak van der Waals bonds of the product. Thus, through adding urea to the mixed precursors, it was more accessible to obtain the smaller-sized nanoparticle products. When it comes to the CMCN, the diffraction peak at 27.6° shifted to 27.4° compared with MCN, indicating that with the presence of cyanuric acid, the lattice plane distance was increased.

The molecular structure of MCN, UMCN, and CMCN were characterized by Fourier transform infrared (FTIR) spectrometry, and the FTIR spectra are shown in Figure 2. The similar absorption peaks of all samples further confirmed the basic molecular composition of $g\text{-C}_3\text{N}_4$. The strong absorption peak at 815 cm^{-1} corresponds to the vibration of the triazine units, which could be formed through the polymerization of cyanic acid in the gaseous phase [33]. The absorption bands within the $1100\text{--}1700\text{ cm}^{-1}$ region correspond to C–N and C=N stretching modes of N-containing heterocycles. The absorption peaks

between 3000–3500 cm^{-1} were assigned to the stretching vibration of uncondensed terminal amino N–H bonds. The spectral bands around 3500 cm^{-1} correspond to the stretching vibrations of –OH groups. It is noted that the intensity of the absorption peak of UMCN between 3000–3500 cm^{-1} corresponding to the related amino groups was more enhanced than that of the MCN, which implies that a large number of amino groups were introduced onto the surface of the $g\text{-C}_3\text{N}_4$ during the thermal polymerization process. As for CMCN, the broadened absorption peak between 3000–3500 cm^{-1} implies the relatively lower content of the N–H groups and probably introduced more –OH groups or oxygen containing groups.

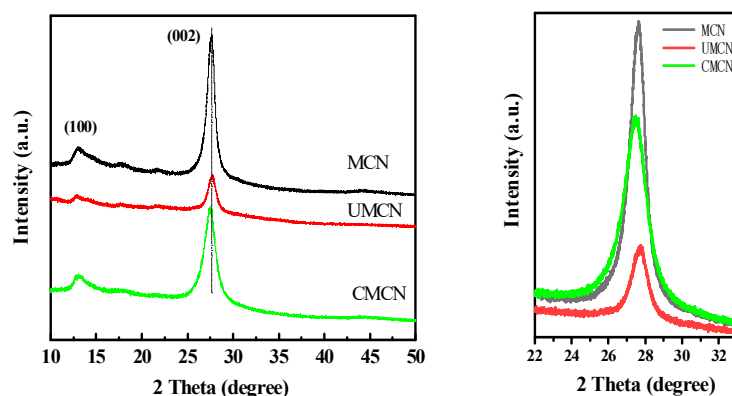


Figure 1. XRD patterns of the samples MCN, UMCN, and CMCN.

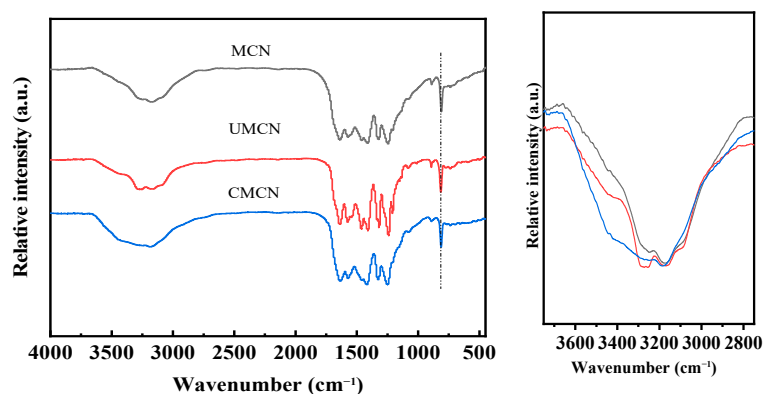


Figure 2. FT-IR spectra of the samples MCN, UMCN, and CMCN.

The morphology and microstructure of MCN, UMCN, and CMCN were investigated by SEM. Figure 3a illustrates that the MCN consisted of a large number of blocky structures, which had some folds on it. As shown in Figure 3b–d, both UMCN and CMCN displayed one-dimensional tubular structures. The UMCN nanotubes had a diameter of 200 nm, while the CMCN nanotubes had a diameter around 100 nm. The one-dimensional tubular structure was formed because urea was first converted into cyanuric acid in situ during calcination, and further formed cyanamine-cyanuric acid supramolecular polymer nanorods through hydrogen bonding with melamine. The similar nanorods were formed when a mixture of melamine and cyanuric acid was heated [34]. One-dimensional nanotubes can enhance the absorption of incident light and promote carrier migration along 1D length, thus promoting effective carrier separation. The exposed inner and outer surfaces of nanotubes had larger specific surface areas, thus providing more catalytic active sites [35]. Figure 3c shows that a large number of holes were distributed on the CMCN nanotubes, which were formed due to the release of gases during the formation of $g\text{-C}_3\text{N}_4$ nanotubes [36]. Scheme 1 illustrates the nanotube microstructure formation of $g\text{-C}_3\text{N}_4$ through one-pot thermal decomposition with different precursor controlling. In addition,

porous g-C₃N₄ had better photocatalytic properties due to its larger surface area and many channels that facilitated mass diffusion [37]. There are many reported porous structures and the preparation is summarized in Table 1.

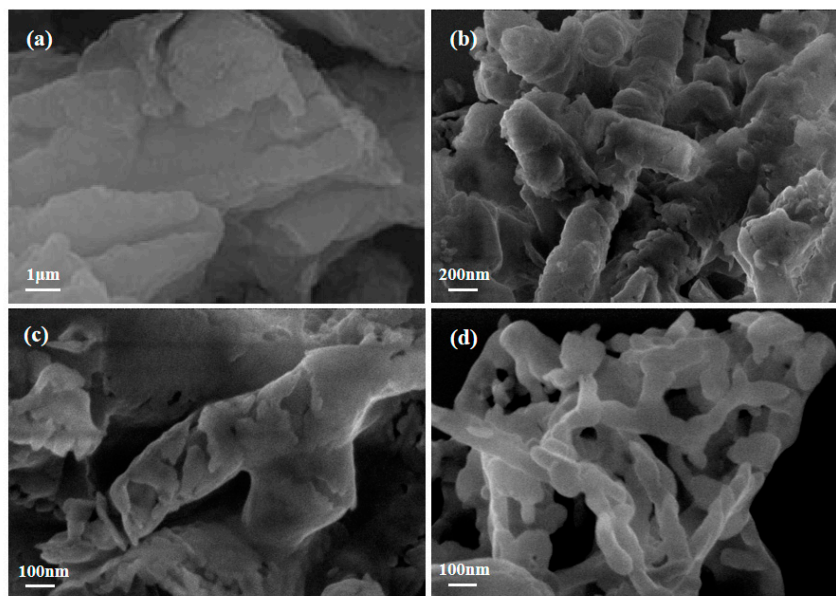
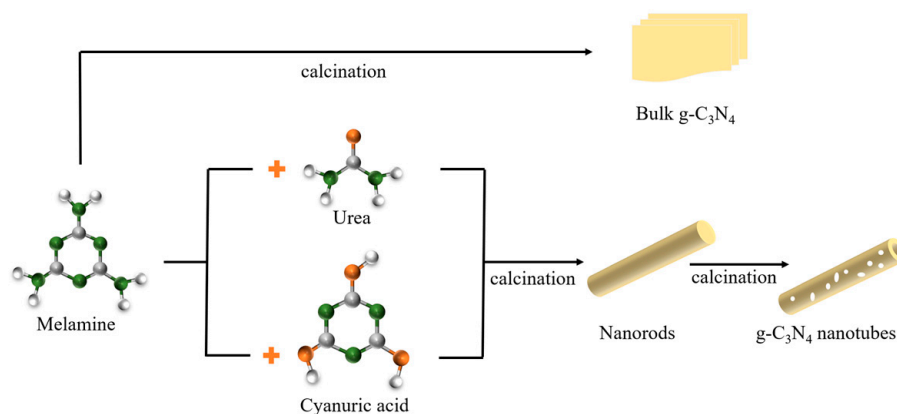


Figure 3. SEM images of MCN (a), UMCN (b,c), and CMCN (d).



Scheme 1. The formation of g-C₃N₄ nanotubes by one-pot thermal decomposition.

Table 1. Summary of reported porous structure and the preparation method.

Porous Structure	Precursor	Method	Ref.
Short rod-like	Dicyandiamide with SBA-15 template	High pressure and High temperature (HPHT) process	[38]
Nanosheets	Melamine and ammonium bicarbonate	Solid-state reaction	[39]
Crafted 1D mesoporous microtubes	Dicyandiamide	Liquid-liquid interfacial self-assembly strategy	[40]
Nanotube	Melamine and urea	Thermal polymerization	This work
Nanotube	Melamine and cyanuric acid	Thermal polymerization	This work

The BET surface area, pore volume, and average pore size of MCN, CMCN, and UMCN are summarized in Table 2. The BET surface area of UMCN is 98.04 m²/g, which is

more than 8 times more than that of CMCN and MCN. Meanwhile, the total pore volume of MCN is $0.10 \text{ cm}^3/\text{g}$, while it increased to $0.58 \text{ cm}^3/\text{g}$ for UMCN. The results imply that the UMCN could possess the best adsorption ability and more active sites for the photocatalytic degradation.

Table 2. BET surface area, pore volume, and average pore size of MCN, CMCN, and UMCN.

Samples	MCN	CMCN	UMCN
BET surface area (m^2/g)	11.15	11.87	98.04
Total pore volume (cm^3/g)	0.10	0.12	0.58
Average pore size (nm)	36.31	40.01	23.68

The photoabsorption ability was analyzed using UV–vis diffused reflectance spectroscopy. As shown in Figure 4a, the UMCN and CMCN displayed a distinct blue shift of the intrinsic absorption edge compared with that of bulk $\text{g-C}_3\text{N}_4$, which may be caused by the quantum confinement effect due to the nanostructure properties of $\text{g-C}_3\text{N}_4$. According to the Kubelka–Munk method, the energy band gaps of the MCN, CMCN, and UMCN were estimated to be 2.47, 2.49, and 2.57 eV, respectively.

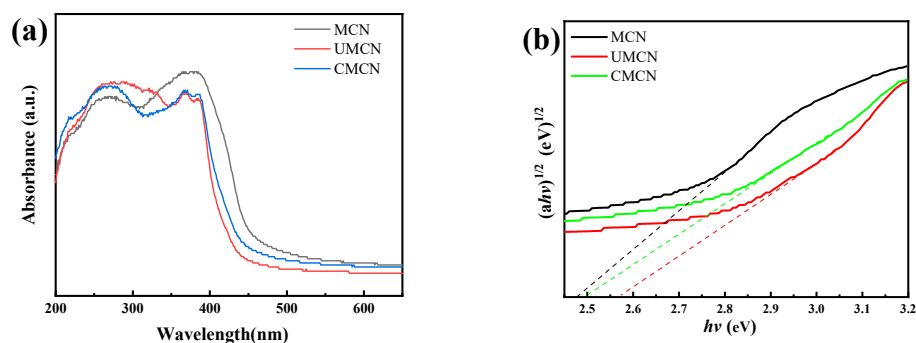


Figure 4. (a) UV–vis diffuse reflectance spectra (b) corresponding plots of $(\alpha hv)^{1/2}$ vs. photon energy of $\text{g-C}_3\text{N}_4$ prepared with different precursors.

2.2. Thermal Decomposition Process Analysis

Figure 5 shows the TG and DTG curves of the annealing of different precursors under the nitrogen atmosphere. Figure 5a,b shows the TG and DTG curves of MCN. There was only one obvious weight loss in the decomposition of the melamine precursor, and the weight loss increased significantly when the temperature was over $210 \text{ }^\circ\text{C}$, which was due to the polycondensation of melamine to form melam and melem. For the generating of $\text{g-C}_3\text{N}_4$, the melamine precursor initially occurred through deamination to form melam and melem [41,42]. When the temperature was over $420 \text{ }^\circ\text{C}$, the mass change rate of the DTG curves (Figure 5b) were close to zero. Figure 5c displays the TG curves of UMCN, which used a mixture of urea and melamine as precursor, with corresponding DTG curves (In Figure 5d). Figure 5c shows three obvious weight losses in the TG curve, indicating more stages of pyrolysis. Compared with MCN using the single melamine as precursor, the initial decomposition process under the temperature ranged from about 130 to $210 \text{ }^\circ\text{C}$. The first weight loss could be attributed to the polycondensation of urea in the UMCN for the formation of biuret. After the first sharp peak, more weak peaks appeared. The following weight loss could be attributed to the polymerization of the forming melamine, which further formed melam and melem at about $380 \text{ }^\circ\text{C}$, and then deaminated to form $\text{g-C}_3\text{N}_4$. During the decomposition processes, NH_3 or HNCO were released. The CMCN samples displayed a weak weight loss under the temperature of 225 – $250 \text{ }^\circ\text{C}$ and a sharp weight loss when the temperature was over $250 \text{ }^\circ\text{C}$. In the second decomposition process, the melamine underwent thermal polymerization to form melam and melem.

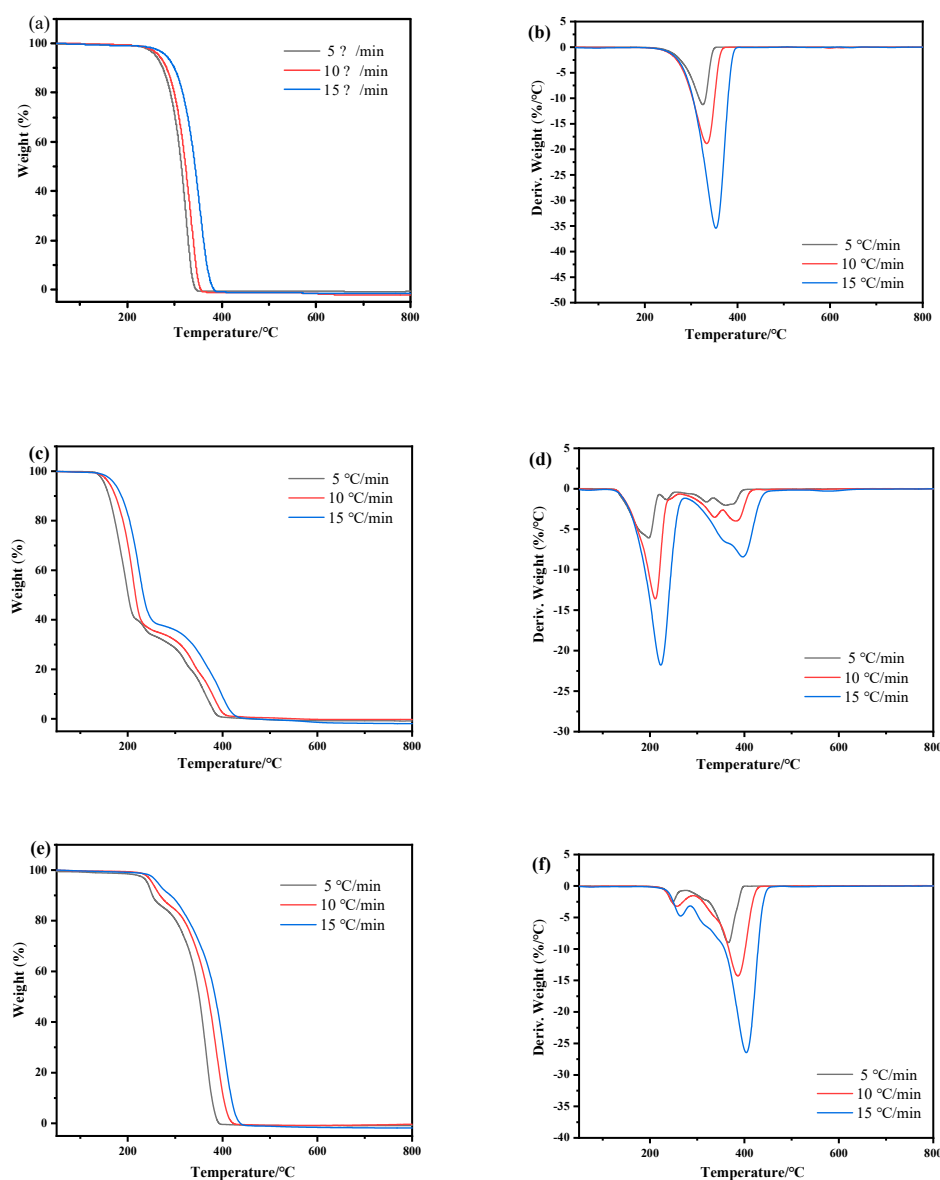


Figure 5. TG–DTG curves of MCN (a,b), UMCN (c,d), and CMCN (e,f).

In order to understand the relationship and interaction between the precursor and the targeted catalyst, the decomposition process of MCN, UMCN, and CMCN was analyzed using thermal decomposition kinetics. The thermal decomposition with different heating rates were measured (5 °C, 10 °C, and 20 °C) to obtain the decomposition kinetics. The model-free method without predicting the reaction mechanism was adopted due to the unknown reaction model of complex reactions. Therefore, the Flynn–Wall–Ozawa method (FWO) was used to summarize the thermal decomposition characteristics. The FWO method was used to calculate the activation energy E . The formula is as follows:

$$\lg\beta = \lg(AE/RG(\alpha)) - 2.315 - 0.4567E/RT$$

where β is the heating rate, R is the gas constant, α is the extent of reaction, $G(\alpha)$ is an integral form of the kinetic function, and A is the pre-exponential factor. For different heating rates at a constant α , the value of activation energy E can be calculated from the slope of the straight line of the plot $\lg\beta$ vs. $1/T$. The conversion rate α is generally 0.1, 0.2, 0.3, 0.4, 0.5, 0.6, 0.7, 0.8, 0.9. In Figure 6, the dependence of activation energy on the extent of conversion for MCN, UMCN, and CMCN using Friedman’s method is displayed.

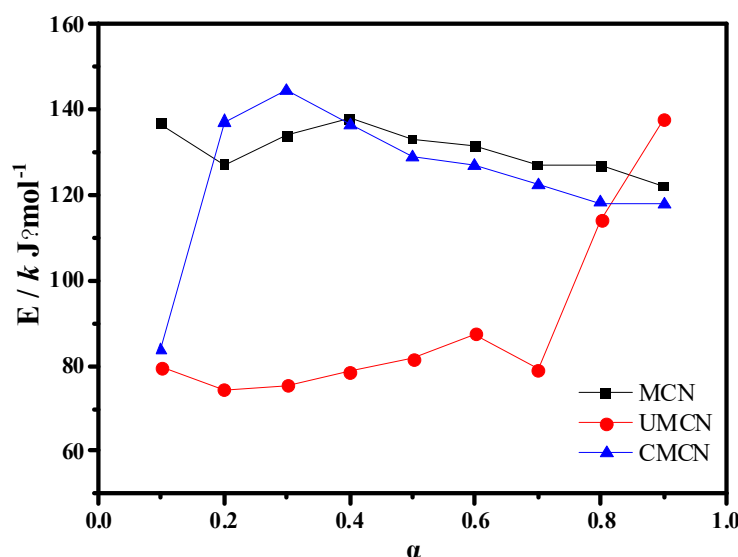


Figure 6. Dependence of activation energy on the conversion rate α for MCN, UMCN, and CMCN.

Activation energy E for thermal decomposition implies the magnitude of reaction resistance and difficulty of the decomposition process, which is increased with the increase of reaction resistance. For MCN, the activation energy changed slightly with the conversion rate, which indicated that the dissociation process could be a simple one-step process. Compared with that of MCN and CMCN, the thermal decomposition activation energy of UMCN sustained a lower level when the conversion was under 0.7. Then UMCN required higher activation energy when the conversion was higher than 0.8. The results indicate that, as for UMCN, there could be a distinct space steric effect when the conversion increased to higher than 0.8, which made the reaction resistance increase and caused the melamine to melam conversion process to be more difficult.

2.3. Photocatalytic Activity of Samples Prepared by Different Precursors

The UV-vis absorption spectrum and molecular formula of NOR is shown in Figure 7a, which is a combination with a benzene ring and a conjugate double bond. The absorption spectra (Figure 7a) were obtained by scanning λ between 232–358 nm. The measured sample had the maximum absorption peak at 273 nm, and the excipients had no interference at 273 nm. NOR is a third-generation fluoroquinolone antibiotic. As a colorless organic pollutant, it can exclude the photosensitization of colored dyes and further evaluate the photocatalytic properties of the material. The main structure of NOR includes the piperazine part and the quinolone part. The benzene rings in these two parts have the highest electron density value. NOR antibiotics can be adsorbed on the surface of the adsorbent by the electrostatic gravity, van der Waals force, and ion exchange of the adsorbent. At the same time, the fluorine atomic group and carboxyl group can strengthen the adsorption with the adsorbent in water.

The sorption ability for NOR in solution using MCN, UMCN, and CMCN samples in the absence of light was performed in Figure 7b, and the sorption attained desorption and absorption equilibrium within 60 min. The NOR adsorption rate was about 4%, 15%, and 14% using MCN, UMCN, and CMCN, respectively. As a control test, the photolysis effect of NOR under visible-light irradiation was investigated in Figure 7c, and the results indicate that the effect of NOR was minimal. The photocatalytic activity of the MCN, UMCN, and CMCN was evaluated by the degradation of NOR solutions under visible-light irradiation, as shown in Figure 7c. The CMCN and UMCN displayed better photocatalytic activity than MCN. The UMCN possessed outstanding photocatalytic activity for NOR degradation compared with MCN. Using UMCN as the catalyst, the NOR degradation rate attained nearly 54% within 15 min, then the degradation gradually slowed down, eventually

attaining about 92% within 150 min. The pseudo-first-order reaction kinetics model was used to express the degradation rate, and the degradation rate of NOR conformed to the pseudo-first-order reaction kinetics equation:

$$-\ln\left(\frac{C_t}{C_0}\right) = k_{obs} * T$$

where k_{obs} (min^{-1}) is the kinetic rate constant, and the larger the k_{obs} value, the faster the degradation rate; C_0 is the initial concentration of NOR, T is the reaction time. Kinetic fitting was performed on the experimental results, and the apparent reaction rate constant k was shown in Figure 7d. The obtained reaction rate constant k of MCN, UMCN, CMCN was 1.19, 1.50, and 1.21 min^{-1} , respectively. The results indicate that UMCN catalysts possessed the best photocatalytic performance for the degradation of NOR.

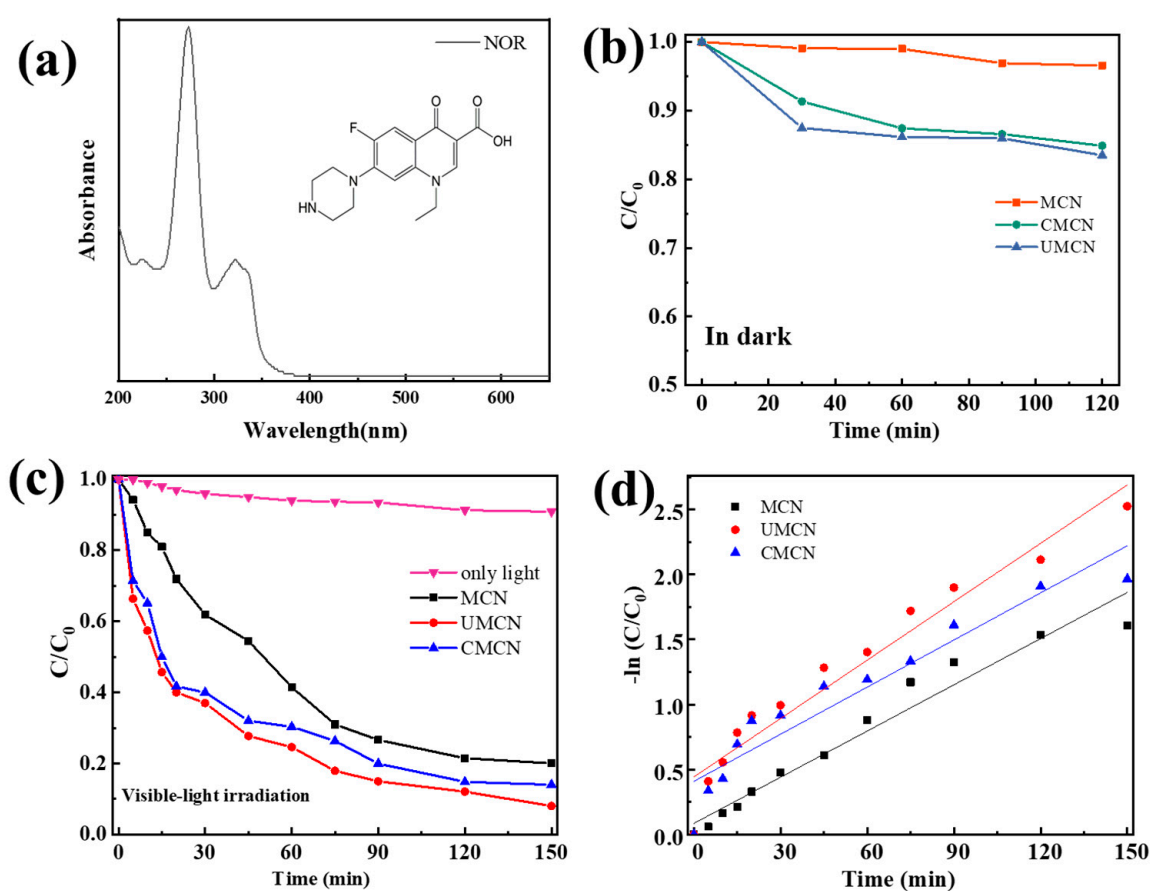


Figure 7. (a) UV-vis absorption spectrum and (inset) the molecular formula of NOR, (b) adsorption ability for NOR using MCN, UMCN, and CMCN samples in the dark, (c) photocatalytic efficiency, and (d) corresponding reaction kinetics as a function of time using MCN, UMCN, and CMCN samples for the removal of NOR under visible-light irradiation.

The photocatalytic performance of UMCN in the NOR solution with different initial pH was evaluated. Generally, as shown in Figure 8a, the UMCN sustained a good degradation efficiency, which indicated the stable performance of UMCN within the solution pH range from 4.5 to 9. To further test its cycling degradation performance, four-cycling degradation is shown in Figure 8b. After the fourth cycle degradation, UMCN sustained a degradation rate of NOR above 75% under visible light irradiation, indicating its potential for a long-term ability.

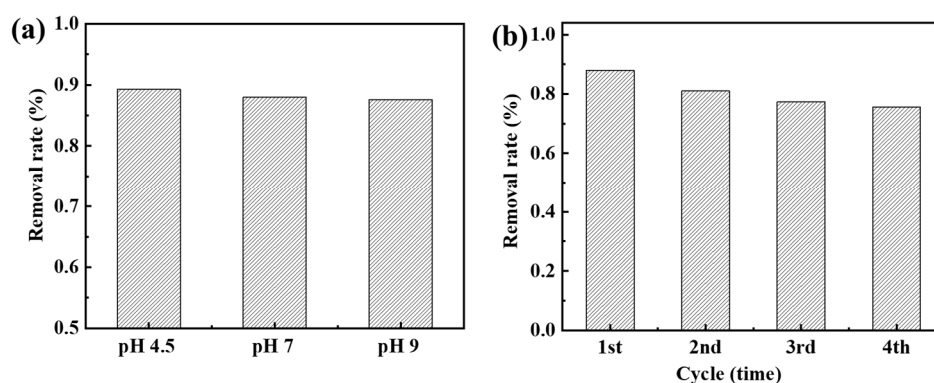
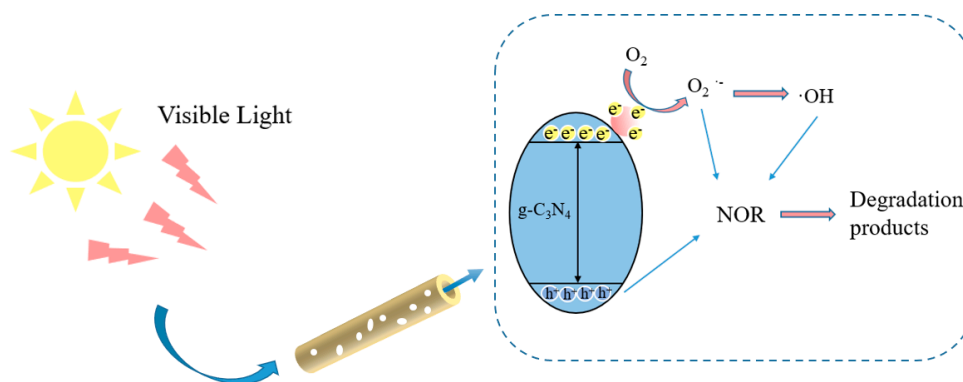


Figure 8. (a) Effects of solution pH on the NOR degradation and (b) cycling tests using UMCN catalysts under 120 min visible light irradiation. (Experimental conditions: NOR concentration = 10 mg/L, photocatalysts amount = 1 g/L).

Scheme 2 illustrates the photocatalytic degradation of NOR solution by $g\text{-C}_3\text{N}_4$ nanotubes. During the photocatalytic reaction, the visible-light excited photogenerated electrons in the CB of $g\text{-C}_3\text{N}_4$ reduce O_2 to $\text{O}_2^{\cdot-}$. In addition, $\cdot\text{OH}$ could be generated via a multistep reaction. Finally, $\text{O}_2^{\cdot-}$ and $\cdot\text{OH}$ as the strong oxygen free radicals facilitated the degradation of NOR. The better photocatalytic performance of UMCN and CMCN could be attributed to their more suitable microstructure. The nanotubular structures provided easier mass transfer efficiency and higher photogenerated charge mobility for the UMCN and CMCN. Furthermore, abundant amino groups on the surface of the UMCN facilitating the formation of reaction active site on the surface for the photocatalytic process.



Scheme 2. The photocatalytic degradation of NOR solution by the $g\text{-C}_3\text{N}_4$ nanotubes.

3. Conclusions

In summary, the $g\text{-C}_3\text{N}_4$ was prepared by a one-pot thermal decomposition process based on controlling precursors. Melamine was used as a N-rich molecular precursor and a mixture with urea or cyanuric acid was also prepared (UMCN and CMCN). The SEM results show that, different from the sheet-like morphology obtained by single precursor melamine, the special one-dimensional nanotube structure of $g\text{-C}_3\text{N}_4$ (the UMCN and CMCN) was obtained by forming supramolecular polymer precursors with a mixture of melamine/urea or cyanuric acid. The exposed surfaces of nanotubes thus created more catalytic active sites for the photocatalytic degradation of NOR. In addition, compared with that of bulk $g\text{-C}_3\text{N}_4$, there more amino groups were retained on the surface of UMCN. The TG-DTG results show that there was more than one obvious weight loss in the decomposition process for UMCN and CMCN. The dissociation involved a multiple-step process. The UMCN and CMCN showed much better photocatalytic performance for the degradation of NOR antibiotics in solution than MCN.

4. Materials and Methods

4.1. Preparation of Catalysts

All chemicals and reagents in the experiment were commercially available and used without further purification. Deionized water was used throughout the experiment. The catalysts were synthesized through a thermal polymerization method. In brief, 5 g melamine was transferred into a 50 mL ceramic crucible with a lid, then heated to 550 °C with a heating rate of 5 °C/min and kept for four hours in a muffle furnace. The yellow residual was ground into a powder using a mortar to obtain g-C₃N₄, denoted as MCN. Meanwhile, different precursors were used to prepare the g-C₃N₄ catalysts, which were prepared with the similar method mentioned above but urea was replaced with a mixture of 5 g urea and 0.5 g melamine, a mixture of 1 g melamine and 5 g cyanuric acid, and denoted as MCN, UMCN, CMCN, respectively.

4.2. Photocatalytic Measurements

Norfloxacin (NOR) was used as model contaminants to investigate the photocatalytic performance of the catalysts for removing organic contaminants. The photocatalytic performance of samples was performed in a 500 mL glass beaker. A parallel photochemical reaction instrument (CEL-LAB200E7, Beijing, China) was used, with 420 nm LED light as visible light source. For each experiment, 50 mg of catalysts were dispersed in 50 mL (10 mg/L) NOR aqueous solution. Prior to visible light irradiation, the reaction solution was stirred for 60 min in the dark to reach an adsorption–desorption equilibrium. At given time intervals, about 2 mL reaction solution was taken through a 0.22 µm cellulose acetate filter, followed by measuring with a UV-vis spectrophotometer (UV-2600, Shimadzu, Kyoto, Japan) at 273 nm to detect the residual NOR concentration. Based on the Lambert–Beer law and the Beer–Lambert law, the pollutant removal rate was calculated by the formula, $Removal\ rate\% = (A_0 - A_t) / A_0 * 100\%$, where the absorbance occurs at the reaction time of 0 min, and A is the instantaneous absorbance during the reaction.

4.3. Characterization

The crystal structures of the catalysts were examined by an X-ray diffractometer (Panalytical X'Pert'3 Powder, Almelo, The Netherlands). The morphology structure of the catalysts was analyzed by scanning electronic micrographs (SEM, Zeiss Sigma 300, Jena, Germany). Fourier transformed infrared spectra (FT-IR) was performed by a Thermo Scientific Nicolet IS20 spectrometer (Waltham, MA, USA). The optical properties of catalysts were analyzed by the UV–vis diffuse reflectance spectra (DRS) test on a spectrometer (Shimadzu UV-2600, Kyoto, Japan). The comprehensive thermal analysis was carried out by a thermogravimetric analyzer (NETZSCH STA 449F3, Bayern, Germany). The samples were placed in the corundum crucible and calcined at the heating rate of 5, 10, 20 °C/min.

Author Contributions: Conceptualization, H.G.; investigation, X.L., X.X. and M.Y.; writing—original draft preparation, X.L., X.X. and M.Y.; writing—review and editing, H.G. and Y.H.; project administration, H.G. and Y.H.; funding acquisition, H.G. and Y.H. All authors have read and agreed to the published version of the manuscript.

Funding: This research was supported by the Zhejiang Provincial Natural Science Foundation of China under grant LY21E090004, National Natural Science Foundation of China under grant 52070103, the Natural Science Foundation of Ningbo under grant 202003N4135, the General Research Project of Zhejiang Provincial Department of Education under grant Y202043966, and K.C. Wong Magna Fund in Ningbo University.

Data Availability Statement: Not applicable.

Conflicts of Interest: The authors declare no conflict of interest.

References

1. Ding, H.J.; Wu, Y.X.; Zhang, W.H.; Zhong, J.Y.; Lou, Q.; Yang, P.; Fang, Y.Y. Occurrence, distribution, and risk assessment of antibiotics in the surface water of Poyang Lake, the largest freshwater lake in China. *Chemosphere* **2017**, *184*, 137–147. [\[CrossRef\]](#)
2. Bilal, M.; Mehmood, S.; Rasheed, T.; Iqbal, H.N. Antibiotics traces in the aquatic environment: Persistence and adverse environmental impact. *Curr. Opin. Environ. Sci. Health* **2020**, *13*, 68–74. [\[CrossRef\]](#)
3. Yu, F.; Li, Y.; Han, S.; Ma, J. Adsorptive removal of antibiotics from aqueous solution using carbon materials. *Chemosphere* **2016**, *153*, 365–385. [\[CrossRef\]](#) [\[PubMed\]](#)
4. Iakovides, I.C.; Michael-Kordatou, I.; Moreira, N.; Ribeiro, A.R.; Fernandes, T.; Pereira, M.; Nunes, O.C.; Manaia, C.M.; Silva, A.; Fatta-Kassinos, D. Continuous ozonation of urban wastewater: Removal of antibiotics, antibiotic-resistant *Escherichia coli* and antibiotic resistance genes and phytotoxicity. *Water Res.* **2019**, *159*, 333–347. [\[CrossRef\]](#)
5. Yin, K.; Deng, L.; Luo, J.; Crittenden, J.; Liu, C.; Wei, Y.F.; Wang, L.L. Destruction of phenicol antibiotics using the UV/H₂O₂ process: Kinetics, byproducts, toxicity evaluation and trichloromethane formation potential. *Chem. Eng. J.* **2018**, *351*, 867–877. [\[CrossRef\]](#)
6. Jiang, Q.J.; Gan, H.H.; Huang, Y.; Lu, D.N.; Yang, Y.Q.; Zhang, W.K. Peroxymonosulfate activation on carbon nano-onions modified graphitic carbon nitride via light-tuning radical and nonradical pathways. *J. Environ. Chem. Eng.* **2021**, *9*, 106592. [\[CrossRef\]](#)
7. Wen, J.Q.; Xie, J.; Chen, X.B.; Li, X. A review on g-C₃N₄-based photocatalysts. *Appl. Surf. Sci.* **2017**, *391*, 72–123. [\[CrossRef\]](#)
8. Sudhaik, A.; Raizada, P.; Shandilya, P.; Jeong, D.Y.; Lim, J.H.; Singh, P. Review on fabrication of graphitic carbon nitride based efficient nanocomposites for photodegradation of aqueous phase organic pollutants. *J. Ind. Eng. Chem.* **2018**, *67*, 28–51. [\[CrossRef\]](#)
9. Zhang, G.G.; Lan, Z.A.; Wang, X.C. Surface engineering of graphitic carbon nitride polymers with cocatalysts for photocatalytic overall water splitting. *Chem. Sci.* **2017**, *8*, 5261–5274. [\[CrossRef\]](#)
10. Zhu, B.C.; Zhang, J.F.; Jiang, C.J.; Cheng, B.; Yu, J.G. First principle investigation of halogen-doped monolayer g-C₃N₄ photocatalyst. *Appl. Catal. B Environ.* **2017**, *207*, 27–34. [\[CrossRef\]](#)
11. Xu, Y.F.; Guo, Q.Q.; Huang, L.; Feng, H.J.; Zhang, C.; Xu, H.Q.; Wang, M.Z. Toward efficient preconcentrating photocatalysis: 3D g-C₃N₄ monolith with isotype heterojunctions assembled from hybrid 1D and 2D nanoblocks. *ACS Appl. Mater. Interfaces* **2019**, *11*, 31934–31942. [\[CrossRef\]](#) [\[PubMed\]](#)
12. Mohazzab, B.F.; Akhundi, A.; Rahimi, K.; Jaleh, B.; Moshfegh, A.Z. P-Doped g-C₃N₄ Nanosheet-Modified BiVO₄ Hybrid Nanostructure as an Efficient Visible Light-Driven Water Splitting Photoanode. *ACS Appl. Energy Mater.* **2022**, *5*, 12283–12296. [\[CrossRef\]](#)
13. Wan, Z.; Zhang, G.K.; Wu, X.Y.; Yin, S. Novel visible-light-driven Z-scheme Bi₁₂GeO₂₀/g-C₃N₄ photocatalyst: Oxygen-induced pathway of organic pollutants degradation and proton assisted electron transfer mechanism of Cr(VI) reduction. *Appl. Catal. B Environ.* **2017**, *207*, 17–26. [\[CrossRef\]](#)
14. Liu, J.; Guo, H.; Yin, H.; Nie, Q.; Zou, S. Accelerated Photodegradation of Organic Pollutants over BiOBr/Protonated g-C₃N₄. *Catalysts* **2022**, *12*, 1109. [\[CrossRef\]](#)
15. Ghanbari, M.; Salavati-Niasari, M. Copper iodide decorated graphitic carbon nitride sheets with enhanced visible-light response for photocatalytic organic pollutant removal and antibacterial activities. *Ecotoxicol. Environ. Saf.* **2021**, *208*, 111712. [\[CrossRef\]](#) [\[PubMed\]](#)
16. Wang, Y.X.; Wang, H.; Chen, F.Y.; Cao, F.; Zhao, X.H.; Meng, S.G.; Cui, Y.J. Facile synthesis of oxygen doped carbon nitride hollow microsphere for photocatalysis. *Appl. Catal. B Environ.* **2017**, *206*, 417–425. [\[CrossRef\]](#)
17. Chebanenko, M.I.; Lebedev, L.A.; Ugolokov, V.L.; Prasolov, N.D.; Nevedomskiy, V.N.; Popkov, V.I. Chemical and structural changes of g-C₃N₄ through oxidative physical vapor deposition. *Appl. Surf. Sci.* **2022**, *600*, 154079. [\[CrossRef\]](#)
18. Wang, Y.G.; Wang, F.; Zuo, Y.H.; Zhang, X.D.; Cui, L.F. Simple synthesis of ordered cubic mesoporous graphitic carbon nitride by chemical vapor deposition method using melamine. *Mater. Lett.* **2014**, *136*, 271–273. [\[CrossRef\]](#)
19. Liu, G.Q.; Xue, M.W.; Liu, Q.P. Facile synthesis of C-doped hollow spherical g-C₃N₄ from supramolecular self-assembly for enhanced photoredox water splitting. *Int. J. Hydrogen Energy* **2019**, *44*, 25671–25679. [\[CrossRef\]](#)
20. Yang, Y.Q.; Jin, H.F.; Zhang, C.; Gan, H.H.; Yi, F.T.; Wang, H.Q. Nitrogen-deficient modified P–Cl co-doped graphitic carbon nitride with enhanced photocatalytic performance. *J. Alloys Compd.* **2020**, *821*, 153439. [\[CrossRef\]](#)
21. Chang, C.; Fu, Y.; Hu, M.; Wang, C.Y. Photodegradation of bisphenol A by highly stable palladium-doped mesoporous graphite carbon nitride (Pd/mpg-C₃N₄) under simulated solar light irradiation. *Appl. Catal. B Environ.* **2013**, *142–143*, 553–560. [\[CrossRef\]](#)
22. Pham, V.V.; Truong, T.K.; Le, H.V.; Nguyen, H.T.; Tong, H.D.; Cao, T.M. Enhancing Green Product Generation of Photocatalytic NO Oxidation: A Case of WO₃ Nanoplate/g-C₃N₄ S-Scheme Heterojunction. *Langmuir* **2022**, *38*, 4138–4146.
23. Tang, Q.; Meng, X.; Wang, Z.; Zhou, J.; Tang, H. One-step electrospinning synthesis of TiO₂/g-C₃N₄ nanofibers with enhanced photocatalytic properties. *Appl. Surf. Sci.* **2018**, *430*, 253–262. [\[CrossRef\]](#)
24. Liang, Q.H.; Li, Z.; Huang, Z.H.; Kang, F.; Yang, Q.H. Holey graphitic carbon nitride nanosheets with carbon vacancies for highly improved photocatalytic hydrogen production. *Adv. Funct. Mater.* **2015**, *25*, 6885–6892. [\[CrossRef\]](#)
25. Bai, X.J.; Wang, L.; Zong, R.L.; Zhu, Y.F. Photocatalytic activity enhanced via g-C₃N₄ nanoplates to nanorods. *J. Phys. Chem. C* **2013**, *117*, 9952–9961. [\[CrossRef\]](#)
26. Yang, Y.; Chen, J.; Mao, Z.; An, N.; Wang, D.; Fahlman, B.D. Ultrathin g-C₃N₄ nanosheets with an extended visible-light-responsive range for significant enhancement of photocatalysis. *RSC Adv.* **2017**, *7*, 2333–2341. [\[CrossRef\]](#)

27. Monga, D.; Ilager, D.; Shetti, N.P.; Basu, S.; Aminabhavi, T.M. 2D/2d heterojunction of MoS₂/g-C₃N₄ nanoflowers for enhanced visible-light-driven photocatalytic and electrochemical degradation of organic pollutants. *J. Environ. Manag.* **2020**, *274*, 111208. [[CrossRef](#)]
28. Wang, Z.; Chen, M.; Yu, H.; Shi, X.; Zhang, Y. Self-Assembly Synthesis of Boron-Doped Graphitic Carbon Nitride Hollow Tubes for Enhanced Photocatalytic NO_x Removal under Visible Light. *Appl. Catal. B Environ.* **2018**, *239*, 55–59. [[CrossRef](#)]
29. Jin, X.D.; Zhou, X.Q.; Sun, P.; Lin, S.Y.; Cao, W.B.; Li, Z.F.; Liu, W.X. Photocatalytic degradation of norfloxacin using N-doped TiO₂: Optimization, mechanism, identification of intermediates and toxicity evaluation. *Chemosphere* **2019**, *237*, 124433. [[CrossRef](#)]
30. Danner, M.C.; Robertson, A.; Behrends, V.; Reiss, J. Antibiotic pollution in surface fresh waters: Occurrence and effects. *Sci. Total Environ.* **2019**, *664*, 793–804. [[CrossRef](#)]
31. Guo, S.; Yang, Z.X.; Zhang, H.L.; Yang, W.; Li, J.; Zhou, K. Enhanced photocatalytic degradation of organic contaminants over CaFe₂O₄ under visible LED light irradiation mediated by peroxymonosulfate. *J. Mater. Sci. Technol.* **2021**, *62*, 34–43. [[CrossRef](#)]
32. Cao, S.H.; Chen, H.; Jiang, F.; Wang, X. Nitrogen photofixation by ultrathin amine-functionalized graphitic carbon nitride nanosheets as a gaseous product from thermal polymerization of urea. *Appl. Catal. B Environ.* **2018**, *224*, 222–229. [[CrossRef](#)]
33. Zhang, J.S.; Chen, Y.; Wang, X.C. Two-dimensional covalent carbon nitride nanosheets: Synthesis, functionalization, and applications. *Energy Environ. Sci.* **2015**, *8*, 3092–3108. [[CrossRef](#)]
34. Wang, X.S.; Zhou, C.; Shi, R.; Liu, Q.Q.; Waterhouse, G.I.N.; Wu, L.Z.; Tung, C.H.; Zhang, T. Supramolecular precursor strategy for the synthesis of holey graphitic carbon nitride nanotubes with enhanced photocatalytic hydrogen evolution performance. *Nano Res.* **2019**, *12*, 2385–2389. [[CrossRef](#)]
35. Yan, X.X.; Jia, Z.Y.; Che, H.B.; Chen, S.Q.; Hu, P.; Wang, J.S.; Wang, L.Z. A selective ion replacement strategy for the synthesis of copper doped carbon nitride nanotubes with improved photocatalytic hydrogen evolution. *Appl. Catal. B Environ.* **2018**, *234*, 15–25. [[CrossRef](#)]
36. Han, Q.; Wang, B.; Gao, J.; Cheng, Z.H.; Zhao, Y.; Zhang, Z.P.; Qu, L.T. Atomically thin mesoporous nanomesh of graphitic C₃N₄ for high-efficiency photocatalytic hydrogen evolution. *ACS Nano* **2016**, *10*, 2745–2751. [[CrossRef](#)] [[PubMed](#)]
37. Ran, J.R.; Ma, T.Y.; Gao, G.P.; Du, X.W.; Qiao, S.Z. Porous P-doped graphitic carbon nitride nanosheets for synergistically enhanced visible-light photocatalytic H₂ production. *Energy Environ. Sci.* **2015**, *8*, 3708–3717. [[CrossRef](#)]
38. Yang, Z.X.; Chu, D.L.; Jia, G.R.; Yao, M.G.; Liu, B.B. Significantly narrowed bandgap and enhanced charge separation in porous, nitrogen-vacancy red g-C₃N₄ for visible light photocatalytic H₂ production. *Appl. Surface Sci.* **2020**, *504*, 144407. [[CrossRef](#)]
39. Zhang, R.; Zhang, X.M.; Liu, S.W.; Tong, J.W.; Kong, F.; Sun, N.K.; Han, X.L.; Zhang, Y.L. Enhanced photocatalytic activity and optical response mechanism of porous graphitic carbon nitride (g-C₃N₄) nanosheets. *Mater. Res. Bull.* **2021**, *140*, 111263. [[CrossRef](#)]
40. Liu, Q.; Chen, C.C.; Yuan, K.J.; Sewell Chris, D.; Zhang, Z.G.; Fang, X.M.; Lin, Z.Q. Robust route to highly porous graphitic carbon nitride microtubes with preferred adsorption ability via rational design of one-dimension supramolecular precursors for efficient photocatalytic CO₂ conversion. *Nano Energy* **2020**, *77*, 105104. [[CrossRef](#)]
41. Lotsch, B.V.; Dobliger, M.; Sehnert, J.; Seyfarth, L.; Senker, J.; Oeckler, O.; Schnick, W. Unmasking melon by a complementary approach employing electron diffraction, solid-state NMR spectroscopy, and theoretical calculations-structural characterization of a carbon nitride polymer. *Chem. Eur. J.* **2007**, *13*, 4969–4980. [[CrossRef](#)] [[PubMed](#)]
42. Thomas, A.; Fischer, A.; Goettmann, F.; Antonietti, M.; Muller, J.O.; Schlogl, R.; Carlsson, J.M. Graphitic carbon nitride materials: Variation of structure and morphology and their use as metal-free catalysts. *J. Mater. Chem.* **2008**, *18*, 4893–4908. [[CrossRef](#)]

Disclaimer/Publisher’s Note: The statements, opinions and data contained in all publications are solely those of the individual author(s) and contributor(s) and not of MDPI and/or the editor(s). MDPI and/or the editor(s) disclaim responsibility for any injury to people or property resulting from any ideas, methods, instructions or products referred to in the content.